parable to the bulk material, and, in the regime where segmental motions are dominant (i.e., in the glassy and early transition regions), the glass transition temperature of the thin films is unchanged within an estimated error of ± 3°C. Calculations using a three-layer viscoelastic model in which the outer two layers have substantially reduced glass transition (15°C) show that the method is sensitive to such layers or gradients when the layer is about 10% or more of the film thickness. The rubbery compliance shows a much reduced value at 27.5 nm, although this is seen to increase as the film thickness increases. It is possible that at this thickness (27.5 nm) the material responds in a different manner to the bulk, perhaps because of a change in the chain conformation (*30*) or because the entanglement density is affected by the constraint imposed by the thickness. However, recent work (*31*) suggests that the entanglement density is reduced in thin films, which would increase the compliance. As such, the observation of a reduced rubbery plateau is surprising and cannot be reconciled within our current understanding of the behavior of ultrathin films. We do not think that it is an artifact of the experiment, e.g., due to surface tension effects or prestrain on the sample caused by the drawing of the film into the hole. At the nanoscale, surface tension effects could become important, but our calculations suggest these effects would be less than 15% for a film of 27.5-nm thickness at the pressure used here.

The effect of prestrain on the sample was estimated by using classical rubber elasticity theory (*32*). Such an analysis implies that a prestrain of about 760% ($\lambda = 7.6$) would be needed to account for the apparent decrease in compliance for the bubble growth data. This is much less than the 25% prestrain estimated because of the capillary draw that occurs during the annealing step in the film preparation.

Comparison of our results to bulk data indicates that there is no significant change in the glass transition temperature down to a thickness of 27.5 nm. This is contrary to results reported for free-standing polystyrene (PS) films, where decreases of up to 70°C for such a thickness have been reported (*23*). However, recent results for poly(methyl methacrylate) (PMMA) (*33*) show a much smaller effect of film thickness on T_g. In this context, the current results would support the possibility that the effect of film thickness on T_g is not universal (*34*). Unexpectedly, whereas the material exhibits a glassy compliance comparable to the bulk data, the rubbery plateau compliance is seen to decrease with decreasing film thickness, indicating stiffening of the rubbery response in the ultrathin film. Future investigations of PS and other polymer films will further explore how the difference in results varies with material chemical structure and how the measurement type (pseudothermodynamic versus dynamic) may impact the interpretation of results.

References and Notes

1. P. W. Anderson, *Science* **267**, 1615 (1995).
2. C. A. Angell, K. L. Ngai, G. B. McKenna, P. F. McMillan, S. W. Martin, *J. Appl. Phys.* **88**, 3113 (2000).
3. C. L. Jackson, G. B. McKenna, *J. Non-Cryst. Solids* **131-133**, 221 (1991).
4. J. A. Forrest, *Eur. Phys. J. E* **8**, 261 (2002).
5. D. Johannsmann, *Eur. Phys. J. E* **8**, 257 (2002).
6. S. L. Simon, J. Y. Park, G. B. McKenna, *Eur. Phys. J. E* **8**, 209 (2002).
7. S. D. Kim, J. M. Torkelson, *Macromolecules* **35**, 5943 (2002).
8. I. Raptis, C. D. Diakoumakos, *Microelectron. Eng.* **61-2**, 829 (2002).
9. R. Kugler, W. Knoll, *Macromol. Chem. Phys.* **203**, 923 (2002).
10. T. S. Chow, *J. Phys. Condens. Matter* **14**, 1333 (2002).
11. G. B. McKenna, *J. Phys. IV* (*Paris*) **10**(P7), 53 (2000).
12. J. Y. Park, G. B. McKenna, *Phys. Rev. B* **61**, 6667 (2000).
13. W. E. Wallace, J. H. van Zanten, W. L. Wu, *Phys. Rev. E* **52**, R3329 (1995).
14. J. L. Keddie, R. A. L. Jones, R. A. Cory, *Faraday Discuss. Chem. Soc.* **98**, 219 (1994).
15. W. J. Orts, J. H. van Zanten, W. L. Wu, S. K. Satija, *Phys. Rev. Lett.* **71**, 867 (1993).
16. C. K. Buenviaje, S.-R. Ge, M. H. Rafailovich, R. M. Overney, in *Fundamentals of Nanondentation and Nanotribology Symposium* (Materials Research Society, Warrendale, PA, 1998), p. 187.
17. K. Dalnoki-Veress, B. G. Nickel, C. Roth, J. R. Dutcher, *Phys. Rev. E* **59**, 2153 (1999).
18. C. G. Yuan, O. Y. Meng, J. T. Koberstein, *Macromolecules* **32**, 2329 (1999).
19. A. E. Green, J. E. Adkins, *Large Elastic Deformations* (Oxford Univ. Press, London, 1970).
20. A. S. Wineman, *Trans. Soc. Rheol.* **20**, 203 (1976).
21. D. D. Joye, G. W. Poehlein, C. D. Denson, *Trans. Soc. Rheol.* **16**, 421 (1972).
22. O. Hassager, S. B. Kristensen, J. R. Larsen, J. Neergaard, *J. Non-Newtonian Fluid Mech.* **88**, 185 (1999).
23. J. Mattson, J. A. Forrest, L. Börjesson, *Phy. Rev. E* **62**, 5187 (2000).
24. Aquamarijn Micro Filtration B.V., Berkelkade 11, 7201 JE Zutphen, Netherlands.
25. M. R. VanLandingham, J. S. Villarrubia, W. F. Guthrie, G. F. Meyers, *Macromol. Symp.* **167**, 15 (2001).
26. K. L. Johnson, *Contact Mechanics* (Cambridge Univ. Press, Cambridge, 1985).
27. H. Lu, B. Wang, J. Ma, G. Huang, H. Viswanathan, *Mech. Time Dependent Mater.* **7**, 189 (2003).
28. D. J. Plazek, *Polym. J.* **12**, 43 (1980).
29. L. Boltzmann, *Sitzungsber. Akad. Wiss. Wien Math. Naturwiss. Kl.* **70**(2), 275 (1874).
30. R. L. Jones, S. K. Kumar, D. L. Ho, R. M. Briber, T. P. Russell, *Macromolecules* **34**, 559 (2001).
31. S. Lun, M. V. Massa, K. Dalnoki-Veress, H. R. Brown, R. A. L. Jones, *Phys. Rev. Lett.*, in press.
32. L. R. G. Treloar, *The Physics of Rubber Elasticity* (Clarendon, Oxford, ed. 3, 1975).
33. C. B. Roth, J. R. Dutcher, *Eur. Phys. J. E* **12**(suppl. 1), S103 (2003).
34. G. B. McKenna, *Eur. Phys. J. E* **12**(1), 191 (2003).
35. M. L. Williams, R. F. Landel, J. D. Ferry, *J. Am. Chem. Soc.* **77**, 3701 (1955).

36. Thanks to the John R. Bradford Endowment at Texas Tech, the National Science Foundation (grant DMR-0304640), and the U.S. Army Research Office (grant W911NF-04-1-0207) for partial support of this project.

24 September 2004; accepted 3 February 2005
10.1126/science.1105658

The Controlled Evolution of a Polymer Single Crystal

Xiaogang Liu,[1]* Yi Zhang,[1]* Dipak K. Goswami,[2] John S. Okasinski,[2] Khalid Salaita,[1] Peng Sun,[1] Michael J. Bedzyk,[2]† Chad A. Mirkin[1]‡

We present a method for controlling the initiation and kinetics of polymer crystal growth using dip-pen nanolithography and an atomic force microscope tip coated with poly-DL-lysine hydrobromide. Triangular prisms of the polymer epitaxially grow on freshly cleaved mica substrates, and their in-plane and out-of-plane growth rates can be controlled by raster scanning the coated tip across the substrate. Atomic force microscope images were concomitantly recorded, providing a set of photographic images of the process as it spans the nanometer- to micrometer-length scales as a function of environmental conditions.

Crystallization is an integral part of many processes and essential for the characterization of many materials, including small molecules, nanoclusters, and biological macromolecules (*1*–*5*). For most crystallization processes, the ability to study the process is limited until the crystal reaches a critical size that allows one to observe it with spectroscopic or x-ray diffraction tools. For single-crystal x-ray diffraction (XRD) techniques, the lower limit is on the order of 100 μm^3, depending on composition and x-ray beam conditions (*6*). For spectroscopic tools, the length scale is even larger. Scanning probe microscopy has been used to visualize crystallization processes in situ, but typically in the context of structures growing randomly on a surface from a bulk solution saturated with a feedstock of the molecule involved in crystallization (*7*–*14*). There are no tools that allow

[1]Department of Chemistry and Institute for Nanotechnology, [2]Department of Materials Science and Engineering and Nanoscale Science and Engineering Center, Northwestern University, Evanston, IL 60208, USA.

*These authors contributed equally to this work.
†To whom inquiries pertaining to crystallography should be addressed. E-mail: bedzyk@northwestern.edu
‡To whom all other correspondence should be addressed. E-mail: camirkin@chem.northwestern.edu

one to site-specifically initiate crystal nucleation, control the growth process in a serial manner, and monitor its progress from the nanometer to micrometer scale.

Dip-pen nanolithography (DPN) allows an atomic force microscope (AFM) tip to transport adsorbates to a surface in a controlled manner (*15*–*19*). This technique has allowed researchers to control the nanoscale architecture of a surface and is compatible with both hard and soft materials (*16*). DPN coupled with AFM also can be used as a serial deposition tool to study monolayer formation (*16*). Polylysine, commonly used as a coating on inorganic substrates for the surface attachment of biomolecules and cells in molecular biology studies, is also regarded as a simple model for protein aggregation studies (*20*, *21*). We show how DPN initiates the crystallization of poly-DL-lysine hydrobromide (PLH) on mica [$KAl_2(AlSi_3)O_{10}(OH)_2$, $2M_1$-muscovite] and study and record the growth process from nanometer-sized seeds to larger crystalline structures as a function of environmental conditions.

In a typical experiment, a PLH-coated silicon AFM tip is used as a deposition tool on a freshly cleaved mica substrate in an AFM raster scanning experiment. The AFM was operated in tapping mode, during which the tip is oscillated at a frequency just below its resonant frequency (300 kHz). Tapping-mode AFM is more suitable than contact mode for imaging delicate polymer samples because it is less damaging to the sample (*19*, *22*). A single scan over an 8-by-8-μm region of the mica surface results in the formation of two equilateral triangular prisms (a and b) that are substantially different in size (Fig. 1, panel 1) (*23*). The smaller triangular feature (b) has a 320-nm edge length and is 21.8 nm thick, whereas the larger one (a) has a 1.62-μm edge length and is 16.5 nm thick. The chemical composition of the nanometer- and micrometer-scale triangular islands was confirmed by time-of-flight secondary ion mass spectroscopy, which exhibits the characteristic fragments for PLH (fig. S1). As the tip was scanned across the same area in tapping mode (scan rate, 2 Hz), one could observe the growth of seed crystals and the formation of new ones (compare panels 1 to 6 in Fig. 1). The growth process is very similar from crystal to crystal under these conditions. All observed structures were equilateral triangles, and crystals that were initiated at approximately the same time had nearly identical dimensions after the same number of raster scans. We found that the crystal thickness and edge length increase with the number of scans or tip-substrate contact time (Fig. 2, A and B).

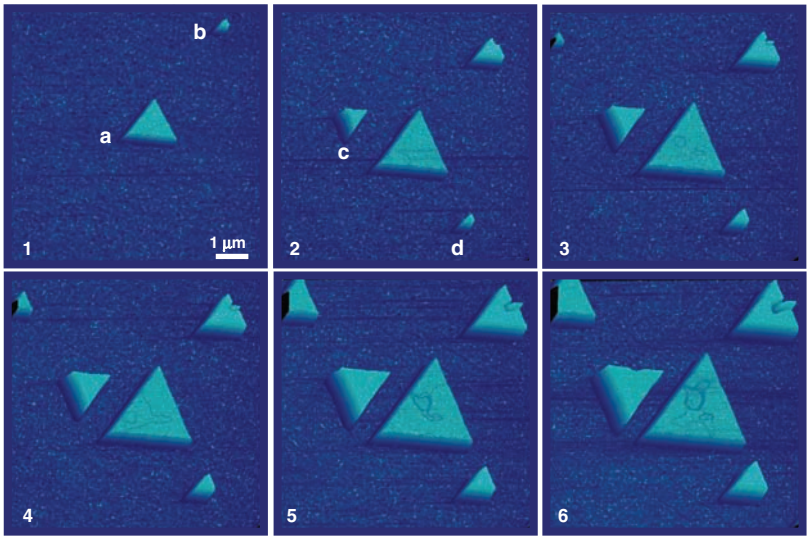

Fig. 1. Panels 1 to 6 show a series of 8-by-8-μm 3D topographic AFM images of mica taken at 256-s intervals (relative humidity, 30%; temperature, 20°C), obtained by continuously scanning an AFM tip coated with PLH molecules in tapping mode (scan rate, 2 Hz). Crystals (labeled as a, b, c, and d) were chosen for kinetic studies. PLH triangles with edge lengths ranging from 100 nm to 10 μm and with heights from 5 to 50 nm were generated. The size of the crystals can be controlled by varying the relative humidity. Lower humidities favor the formation of smaller triangles.

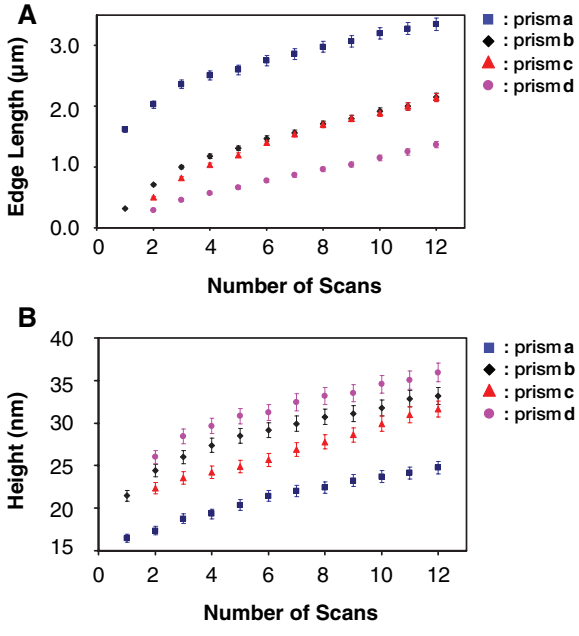

Fig. 2. (**A**) The edge length and (**B**) the height of PLH prisms a to d shown in Fig. 1 plotted as a function of number of raster scans. Error bars show mean ± SD.

Control experiments indicate that it is difficult to grow the well-defined triangular prisms through direct exposure of the mica substrate to a solution containing the PLH. In such control experiments, freshly cleaved mica substrates were either soaked in PLH solutions that varied in concentration (2 to 20 mg/ml) for 3 hours or immersed in the solutions and immediately removed and then stored in a humidity chamber (30% relative humidity) at 20°C for 1 to 2 hours, during which time the solvent evaporated. Many types of microstructures could be observed on the mica surfaces, including amorphous materials and truncated triangles of varying dimensions. Conditions that allowed us to visualize the nucleation process on the nanoscale could not be identified (fig. S2). Similar results were observed when microcontact printing with a polydimethylsiloxane (PDMS) stamp was used to crystallize PLH on mica (*24*).

The data strongly suggest a tip-modulated crystallization process that controls the delivery of the molecules and subsequently the kinetics of crystal growth. The primary role of the tip is in controlling the location of crystallization and a heavy concentration of the crystallizing PLH. The scan direction does not substantially affect the growth process or the orientation of the crystals. Furthermore, the rate of increase for the edge length is substantially faster than that for the thickness. This can be attributed, in part, to the strong electrostatic PLH molecule-substrate interaction (vide infra) that accelerates the growth of the crystal

along its edges. In addition, because of the thin nature of these structures, the number of molecules required to increase the height of a triangle is larger than the number required to extend their edge lengths. This area effect on growth rate is exacerbated as the crystals grow. Another notable feature of this process is that all of the prisms grow in one of two orientations that differ by a 180° rotation, which indicates oriented epitaxial growth of the PLH crystals with respect to the underlying pseudo-hexagonal two-dimensional (2D) lattice of the mica surface (*25*). Indeed, control experiments involving the deposition of PLH on silicon, silicon oxide, highly ordered pyrolytic graphite, and amine-terminated mica substrates do not yield triangular-shaped structures (figs. S3 and S4).

Optical microscopy and single-crystal XRD of the mica substrate with back-reflection Laue and single-crystal diffraction methods were employed to determine the crystallographic orientations of the prisms relative to the substrate. These experiments revealed that the two opposing prism orientations aligned with the mica [100] direction as shown in Fig. 3, A and B, and matched the 2D symmetry of the mica surface (*26*). Consistent with the characterization of the triangular structures as crystals of PLH, drying them results in substantial water loss and morphological change. After drying in air at 20°C for 20 min, the triangular features transformed into uniform triangular frames that maintained an epitaxial relationship with the underlying mica lattice (Fig. 3C). An analysis of the volumes of filled triangles and their corresponding frame structures shows that water makes up about 60% of their volume.

To show that the triangular structures are indeed crystals and to gain a better understanding of their structure and relationship with the underlying mica substrate, single-crystal oscillation XRD patterns were collected in a grazing-incidence geometry at the Advanced Photon Source 5ID-C undulator beamline with the use of a five-circle Huber diffractometer and a MAR 2D charge-coupled device (CCD) area detector (*27*). The PLH 1-by-1-mm^2 area on the mica surface was aligned with the x-ray beam and diffractometer center by observing the Br Kα fluorescence signal from the PLH with an energy-dispersive solid-state x-ray detector. Two separate sets of oscillation patterns were collected from the same sample under identical conditions: one set from the bare mica (i.e., no Br Kα fluorescence) and the other set from the PLH-covered mica. The ϕ rotational axis of the diffractometer was laser aligned with the mica **c*** axis [i.e., perpendicular to (001) cleavage face]. The total contiguous and identical rotational range used for each of the two data sets shown in Fig. 3D is 50°. This is the sum of 50 separate 20-s exposures, each taken over a 1° range in ϕ. The directly measured reciprocal-space coordinates in terms of scattering vector vertical component ($\mathbf{Q_V}$) versus horizontal ($\mathbf{Q_H}$) for the 2D diffraction pattern in Fig. 3D were produced by converting the (*x*, *z*) pixel coordinate of each peak that appeared in the set of CCD frames. The circles in Fig. 3D were observed diffraction spots in both sets (bare and PLH-covered mica) of data and are (hkl) indexed consistent with the monoclinic $2M_1$-muscovite reciprocal lattice. The triangles in Fig. 3D, which were diffraction spots only observed within the PLH set of oscillation patterns, have (hkl) indices that are noninteger, inconsistent with muscovite, and therefore originating from the PLH triangular prisms (table S1). Typical diffraction spots for a particular ϕ collected in the CCD camera are shown in the inset of Fig. 3D. Each diffraction spot occurs only at a particular 1° interval of ϕ. This indicates that the prisms grown on mica are single crystal

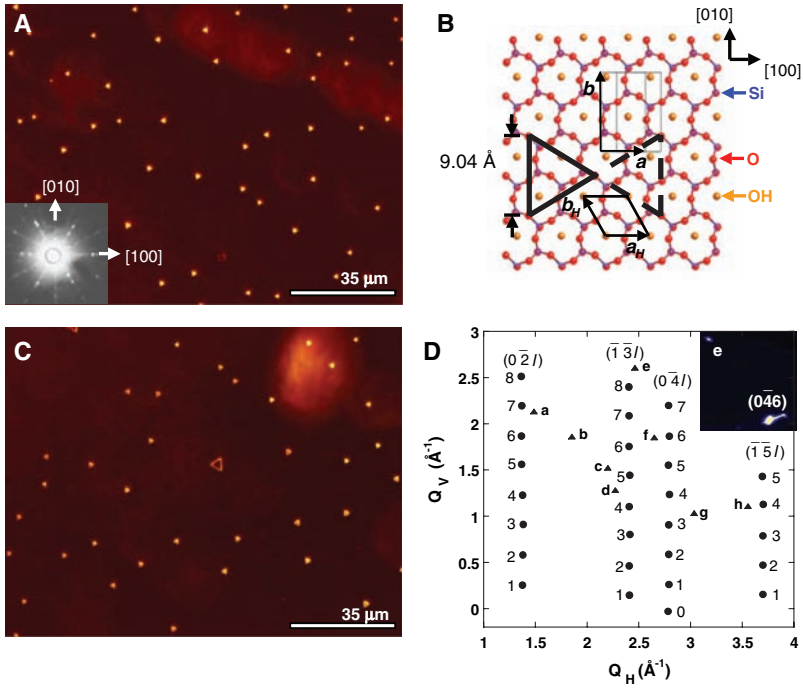

Fig. 3. (**A**) Dark-field light-scattering image of triangular crystals grown by means of the DPN method. (Inset) Laue pattern of the mica substrate. (**B**) Surface arrangement of the uppermost oxygen layer for cleaved mica. Triangles with edge lengths of 9.04 Å show the proposed arrangements of the prisms on the oxygen layer with solid or dashed lines indicating two possible orientations for the PLH prisms. (**C**) Dark-field light-scattering image of triangles upon drying in air for 20 min. (**D**) Single-crystal XRD data from mica (circles) and PLH prisms (triangles labeled a through h). $\mathbf{Q_H}$ and $\mathbf{Q_V}$ are the horizontal and vertical components of the scattering vector, respectively. Each column of mica diffraction spots has the same (*h*, *k*) indices. Each individual spot is marked with the corresponding *l* index. (Inset) A typical CCD image. In this frame, the mica (0 $\bar{4}$ 6) diffraction spot and the PLH prism diffraction spot labeled e appear.

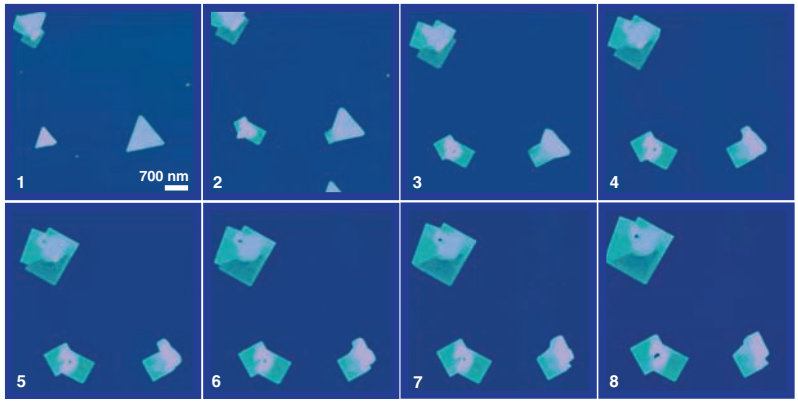

Fig. 4. Panels 1 to 8 show the AFM observed phase transformation of triangular prisms into cubes on mica. Images were taken at 256-s intervals by continuously scanning an AFM tip coated with PLH molecules in tapping mode (scan rate, 2 Hz). The relative humidity was 15% and the temperature was 35°C. The field of panel 2 is slightly offset because of thermal drift.

with a lattice that has an in-plane orientational epitaxy with the underlying mica lattice. The only reason x-ray analysis can be carried out on these structures is because we are able to signal average over a large collection of prisms that are aligned with one another and epitaxially arranged on the mica support.

This approach to controlling and monitoring the kinetics of crystal growth can be used to study environment-imposed changes in crystal morphology (*28*). Subtle changes in temperature markedly affect the growth of the crystals and the observed morphology of the crystals ultimately formed. Indeed, when the temperature is increased to 35°C, cubic-shaped features emerge at the edges of the prisms while scanning the crystals that were preformed at lower temperature with the PLH-coated AFM tip (Fig. 4). This morphological change is very reproducible and always was induced at the corners or edges of the starting triangular crystals.

This study provides an approach for site-specifically initiating crystal growth on the nanometer-length scale in a way that allows one to monitor growth from crystal seed to more mature structures as a function of environmental conditions (fig. S5). The size of the smallest crystal observed and studied in these experiments (d in Fig. 1) is five orders of magnitude smaller than what could be studied by single-crystal XRD techniques, allowing one to observe morphological changes that would typically go undetected in an x-ray study that focuses on larger structures. Finally, growing crystals of macromolecules is not a trivial process. DPN is now a massively parallel tool (*16*, *29*, *30*), suggesting that this study may open the door for creating combinatorial approaches to identifying the proper conditions to initiate a particular type of crystal growth for a given set of target molecules.

References and Notes

1. E. M. Landau, M. Levanon, L. Leiserowitz, M. Lahav, J. Sagiv, *Nature* **318**, 353 (1985).
2. Y. Yin *et al.*, *Science* **304**, 711 (2004).
3. S. Mann, G. A. Ozin, *Nature* **382**, 313 (1996).
4. J. L. Fransaer, R. M. Penner, *J. Phys. Chem. B* **103**, 7643 (1999).
5. S. A. Empedocles, M. G. Bawendi, *Science* **278**, 2114 (1997).
6. J. J. Pluth *et al.*, *Proc. Natl. Acad. Sci. U.S.A.* **94**, 12263 (1997).
7. A. C. Hillier, M. D. Ward, *Science* **263**, 1261 (1994).
8. M. D. Ward, *Chem. Rev.* **101**, 1697 (2001).
9. D. E. Hooks, C. M. Yip, M. D. Ward, *J. Phys. Chem. B* **102**, 9958 (1998).
10. T. A. Land, A. J. Malkin, Y. G. Kuznetsov, A. McPherson, J. J. De Yoreo, *Phys. Rev. Lett.* **75**, 2774 (1995).
11. H. H. Teng, P. M. Dove, C. A. Orme, J. J. De Yoreo, *Science* **282**, 724 (1998).
12. J. K. Hobbs, M. J. Miles, *Macromolecules* **34**, 353 (2001).
13. N. Sanz, J. K. Hobbs, M. J. Miles, *Langmuir* **20**, 5989 (2004).
14. J. K. H. Hörber, M. J. Miles, *Science* **302**, 1002 (2003).
15. R. D. Piner, J. Zhu, F. Xu, S. Hong, C. A. Mirkin, *Science* **283**, 661 (1999).
16. D. S. Ginger, H. Zhang, C. A. Mirkin, *Angew. Chem. Int. Ed. Engl.* **43**, 30 (2004).
17. B. W. Maynor, J. Li, C. Lu, J. Liu, *J. Am. Chem. Soc.* **126**, 6409 (2004).
18. R. J. Barsotti, M. S. O'Connell, F. Stellacci, *Langmuir* **20**, 4795 (2004).
19. G. Agarwal, L. A. Sowards, R. R. Naik, M. O. Stone, *J. Am. Chem. Soc.* **125**, 580 (2003).
20. B. S. Jacobson, D. Branton, *Science* **195**, 302 (1977).
21. W. Dzwolak, R. Ravindra, C. Nicolini, R. Jansen, R. Winter, *J. Am. Chem. Soc.* **126**, 3762 (2004).
22. B. Ratner, V. V. Tsukruk, *Scanning Probe Microscopy in Polymers* (ACS Symposium Series, American Chemical Society, Washington, DC, 1998).
23. The orientation is not related to the tip scanning direction. Change of the orientation of the mica substrate does not change the growth of the prisms or their orientation with respect to each other and the mica.
24. X. Liu *et al.*, data not shown.
25. R. Kern, in *Crystal Growth in Science and Technology*, H. Arend, J. Hulliger, Eds. (Plenum Press, New York, 1989), pp. 143–165.
26. Materials and methods are available as supporting material on *Science* Online.
27. D. A. Walko *et al.*, *AIP Conf. Proc.* **705**, 1166 (2004).
28. W. C. McCrone, in *Physics and Chemistry of Organic Solid State*, D. Fox, M. M. Labes, A. Weissberger, Eds. (Interscience, New York, 1965), pp. 726–767.
29. S. Hong, C. A. Mirkin, *Science* **288**, 1808 (2000).
30. D. Bullen, S. W. Chung, X. Wang, J. Zou, C. A. Mirkin, *Appl. Phys. Lett.* **84**, 789 (2004).

31. Supported by the Nanoscale Science and Engineering Initiative of the NSF under NSF Award No. EEC-0118025, the NIH through Award No. GM62109-02, and a Director's Pioneer Award to C.A.M., the Institute for BioNanotechnology in Medicine, Baxter Healthcare Corp, and the Air Force Office of Scientific Research (AFOSR) through a Multidisciplinary University Research Initiative (MURI) Award.

Supporting Online Material

www.sciencemag.org/cgi/content/full/307/5716/1763/DC1
Materials and Methods
Figs. S1 to S5
Table S1
References

6 January 2005; accepted 3 February 2005
10.1126/science.1109487

The Climate Change Commitment

T. M. L. Wigley

Even if atmospheric composition were fixed today, global-mean temperature and sea level rise would continue due to oceanic thermal inertia. These constant-composition (CC) commitments and their uncertainties are quantified. Constant-emissions (CE) commitments are also considered. The CC warming commitment could exceed 1°C. The CE warming commitment is 2° to 6°C by the year 2400. For sea level rise, the CC commitment is 10 centimeters per century (extreme range approximately 1 to 30 centimeters per century) and the CE commitment is 25 centimeters per century (7 to 50 centimeters per century). Avoiding these changes requires, eventually, a reduction in emissions to substantially below present levels. For sea level rise, a substantial long-term commitment may be impossible to avoid.

Oceanic thermal inertia causes climate change to lag behind any changes in external forcing and causes the response to be damped relative to the asymptotic equilibrium response (*1*–*3*). Because of this lag or damping effect, and because of the changes in atmospheric composition (and radiative forcing) that have already occurred, the climate system will continue to change for many decades (centuries for sea level) even in the absence of future changes in atmospheric composition. For global-mean temperature, this is referred to as the "unrealized warming" (*2*), "residual warming" (*4*), or "committed warming" (*5*). Here, I use the term "warming commitment" or, to include sea level rise (*6*, *7*), "climate change commitment."

The assumption of constant atmospheric composition on which the warming commitment idea is based is clearly unrealistic, even as an extreme case of what might happen in the future. An alternative indicator of the commitment to climate change is to assume that the emissions (rather than concentrations) of radiatively important species will remain constant. This Report investigates the constant-composition (CC) warming and sea level commitments, the constant-emissions (CE) commitments, and the uncertainties in each. Uncertainties arise from uncertainties in the climate sensitivity (*2*, *4*), the rate of ocean heat uptake (*2*), the magnitude of past forcing, and the ice melt contribution to sea level change.

The usual (or "equilibrium") CC warming commitment at time t is the difference between the equilibrium warming for forcing at this time (ΔT_e) and the corresponding realized warming (ΔT_r), $\Delta T_e - \Delta T_r$. This is related to the "radiation-imbalance" concept (*8*, *9*). If ΔQ is the forcing to date, and if ΔQ_r is the forcing that gives an equilibrium warming of ΔT_r, then the radiation imbalance is $\Delta Q - \Delta Q_r$ [$\Delta Q - \Delta Q_r$ is approximately equal to the flux of heat into the ocean (*9*)]. Hence

$$\Delta T_e - \Delta T_r = (\Delta Q - \Delta Q_r)(\Delta T2\times/\Delta Q2\times)$$

where $\Delta Q2\times$ is the radiative forcing for a CO_2 doubling (about 3.7 W/m^2) and $\Delta T2\times$ is the corresponding equilibrium global-mean warming. A central estimate of ΔQ (accounting for both natural and anthropogenic forcings) is about 1.7 W/m^2, whereas ΔT_r is about

National Center for Atmospheric Research, Boulder, CO 80307, USA. E-mail: wigley@cgd.ucar.edu